Article

Irreversible synthesis of an ultrastrong two-dimensional polymeric material

https://doi.org/10.1038/s41586-021-04296-3

Received: 13 January 2021

Accepted: 1 December 2021

Published online: 2 February 2022

Check for updates

Yuwen Zeng[1], Pavlo Gordiichuk[1], Takeo Ichihara[1], Ge Zhang[1], Emil Sandoz-Rosado[2], Eric D. Wetzel[2], Jason Tresback[3], Jing Yang[1], Daichi Kozawa[1], Zhongyue Yang[1], Matthias Kuehne[1], Michelle Quien[1], Zhe Yuan[1], Xun Gong[1], Guangwei He[1], Daniel James Lundberg[1], Pingwei Liu[1], Albert Tianxiang Liu[1], Jing Fan Yang[1], Heather J. Kulik[1] & Michael S. Strano[1]✉

Polymers that extend covalently in two dimensions have attracted recent attention[1,2] as a means of combining the mechanical strength and in-plane energy conduction of conventional two-dimensional (2D) materials[3,4] with the low densities, synthetic processability and organic composition of their one-dimensional counterparts. Efforts so far have proven successful in forms that do not allow full realization of these properties, such as polymerization at flat interfaces[5,6] or fixation of monomers in immobilized lattices[7–9]. Another frequently employed synthetic approach is to introduce microscopic reversibility, at the cost of bond stability, to achieve 2D crystals after extensive error correction[10,11]. Here we demonstrate a homogenous 2D irreversible polycondensation that results in a covalently bonded 2D polymeric material that is chemically stable and highly processable. Further processing yields highly oriented, free-standing films that have a 2D elastic modulus and yield strength of 12.7 ± 3.8 gigapascals and 488 ± 57 megapascals, respectively. This synthetic route provides opportunities for 2D materials in applications ranging from composite structures to barrier coating materials.

Two-dimensional polymers[1,7,12] have long been conceptualized and attempts as early as 1935 explored one-dimensional concatenation of amphiphiles confined to the air–water interface[13]. That work inspired recent advances towards 2D polymers utilizing surface templates[5,14], promising strategies that might enable the release of such materials from the template in a scalable fashion[15]. Similarly, another work first synthesized, by reversible solvothermal crystallization, two covalent organic frameworks that showed layered unit cells stacked in three dimensions[16]. This and other methods, however, have proven difficult to exfoliate or reprocess into engineering materials with useful properties. Reversible synthetic approaches appear to yield materials with limited chemical and mechanical stability such that post-modification or exfoliation is difficult[10,17]. A substantial advance came about recently by utilizing the irreversible nucleophilic aromatic substitutions for 2D polycondensation under solvothermal conditions[18,19]. The resulting bulk powders, unlike previous examples, are chemically stable—pointing to the importance of irreversible bonding in approaching the properties of one-dimensional (1D) polymer systems. By contrast, chemical vapor deposition (CVD) has enabled access to a substantial number of 2D crystalline materials[20], with advantageous in-plane mechanical properties[3]. The high temperatures typically needed for CVD exclude polymerization of organic molecules, and hence 2D organic analogues of 1D polymers have thus far remained elusive. The totality of prior work points to the importance of irreversible chemical routes, necessarily outside of solvothermal or CVD synthetic methods, with strong in-plane bonding such that solution-phase exfoliation is possible.

There are several challenges to homogenous 2D polymerization, but the most fundamental is that for a 2D disc molecule, the number of perimeter addition sites scales with the number of incorporated monomers i, to the power of 1/2. Meanwhile, the three-dimensional (3D) spherical counterpart grows much faster, as $i^{2/3}$ (ref. [21]). This means that as soon as a polymerizing molecular disc grows a defect branch out of the plane, the 3D structure will extend much faster than the desired in-plane 2D disc. Such out-of-plane branches occur easily, with just a single bond rotation of an attached monomer. It is clear that 2D polymerization must fundamentally overcome the high entropic cost of maintaining in-plane bonding. Worse still, irreversible synthetic routes necessarily magnify the effect of single out-of-plane defects with no means of error-correcting[1].

Our reaction design strategy is multifold, and involves an amide condensation of C3-symmetric acid chloride and melamine (Fig. 1a). Our hypothesis is that a strong amide–aromatic conjugation inhibits out-of-plane rotation; meanwhile, the interlayer hydrogen bonding or van der Waals attraction can allow growing discs to absorb monomers from the solution and auto-template them onto 2D surfaces, facilitating the 2D growth pathway (Extended Data Fig. 1). Indeed, chemical kinetic modelling shows that it is possible to produce 2D polymeric materials in excess of 90% yield with a combination of a moderate in-plane to out-of-plane probability ratio (γ), expected from amide conjugation, along with a relative rate constant acceleration (β) from monomers adsorbed onto existing 2D platelets as a form of auto-catalytic self-templating[21]. In our designed reaction system, the

[1]Department of Chemical Engineering, Massachusetts Institute of Technology, Cambridge, MA, USA. [2]U.S. Army Combat Capabilities Development Command, Army Research Laboratory, Aberdeen Proving Ground, MD, USA. [3]Center for Nanoscale Systems, Harvard University, Cambridge, MA, USA. ✉e-mail: strano@mit.edu

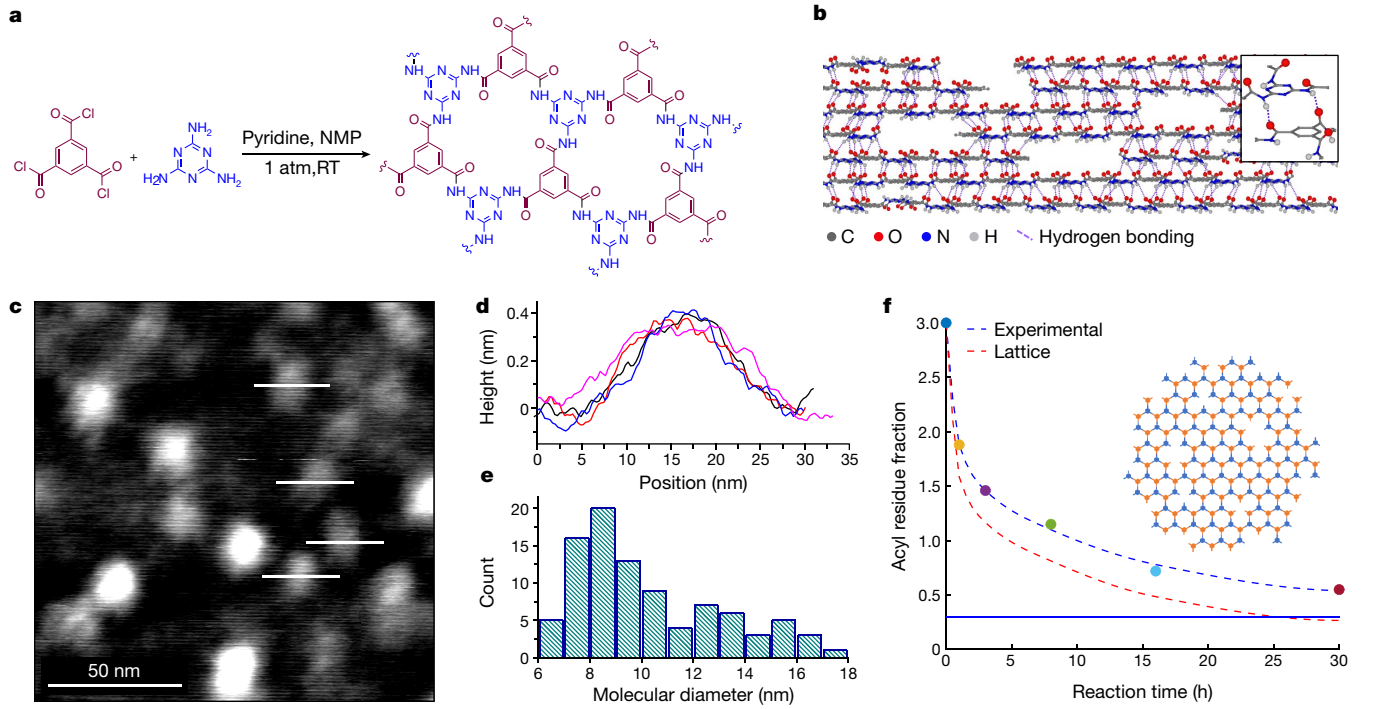

Fig. 1 | Synthesis and characterization of a 2D polymeric material. **a**, Synthetic route to a 2D polyaramid, which we term 2DPA-1. NMP, *N*-methyl-2-pyrrolidone; RT, room temperature. **b**, Cross-sectional view of a proposed hydrogen-bonded, interlocked layered structure. Inset, a close-up of interlayer hydrogen bonds. **c**, High-resolution AFM image of TMS-2DPA-1. Scale bar, 50 nm. **d**, Height profiles along the white lines indicated in **c** (from top to bottom: black, red, blue and pink). **e**, Size distribution of observed TMS-2DPA-1 molecules. **f**, The acyl residue fraction versus reaction time. The blue horizontal line indicates the limit of the residue fraction when molecules grow infinitely large, corresponding to its interior defect density. Inset, a representative 2DPA-1 molecule.

inert amide linkage ensures superb mechanical and chemical stability, allowing sonication and harsh acid or heat treatment. Additionally, triazine cores are intentionally introduced and offer a high density of Lewis bases, leading to protonation in strong acid and thus excellent solubility for high processability.

We indeed find that this irreversible polyaramid chemistry enables 2D condensation in solution phase under ambient conditions, producing high yields of an in-plane bonded polymer, that is, a 2D polyaramid, which we term 2DPA-1 (Fig. 1a). A subsequent Fourier-transform infrared (FTIR) study confirms the formation of amide linkages and highly hydrogen-bonded N–H stretching (Extended Data Fig. 2a). We then characterized 2DPA-1 by atomic force microscopy (AFM) after solution deposition. However, owing to its strong aggregation tendency brought by interlayer hydrogen bonding, bilayer clusters (Extended Data Fig. 2b) and continuous nanosheets (Extended Data Fig. 2c) are observed instead of individual molecules. To shed light on its molecular dimensionality, we prepared silylated 2DPA-1 (Extended Data Fig. 3, Methods section 'Synthesis of TMS-2DPA-1'), because the modification apparently breaks the hydrogen bonding with minimum structural perturbation, leading to discrete molecules. Indeed, TMS-2DPA-1 produces a high ratio of single molecules with distinct heights and lateral dimensions (Fig. 1c). The average molecular thickness and diameter are found to be 3.69 ± 0.28 Å (Fig. 1d) and 10.3 ± 2.8 nm (Fig. 1e), respectively. This monomer-scale thickness is recognized as a definitive signature of 2D polymerization[22].

We further quantified the defect density of 2DPA-1 by measuring its living acyl residues after synthesis, which come from both the molecular periphery and its interior bonding defects. We developed an NMR technique (see Supplementary Information) to estimate this acyl residue-to-monomer ratio, observing that it decreases with increasing reaction time as expected (Fig. 1f), consistent with growing molecular size. Comparing a 10-nm mean diameter of 2DPA-1 to a perfect hexagonal molecule yields an upper estimate of the interior defect density of 0.28 acyl per nm^2 after subtracting the edge acyl contribution, neglecting branched edges with necessarily larger periphery contributions. The calculated average molecular weight based on the observed molecular diameters and defect densities exceeds 20 kDa, comparable to that of 1D polymers.

To realize compelling applications of 2D materials, they must be processable into films and membranes. However, polycrystallinity and poor alignment often hinder this goal[23,24]. The strong aggregation tendency of 2DPA-1 apparently allows uniform and continuous nanometre-thick films to be easily generated by simple spin-coating of a trifluoroacetic acid (TFA) solution onto a flat substrate or even across a microwell. The thickness is well controlled by tuning the solution concentration (Fig. 2a). It is noteworthy that a film can exist less than 4 nm in thickness, indicating that even a few molecular layers have the strength to form an infinitely extended film. All measured films are ultraflat, possessing small apparent r.m.s. (root mean square) roughnesses (approximately 500 pm over 5 × 5 μm^2), corresponding to a height variation of no more than four molecular layers (Extended Data Fig. 2d). We thus conclude that the 2DPA-1 films possess an orientation order with platelets aligning in-plane (Fig. 1b), but staggered such that the internal Brunauer–Emmett–Teller (BET) pore surface area is effectively inaccessible (Supplementary Table 1). We further developed a film transfer method for rough or even holey substrates (Fig. 2b). Such a protocol also enables preparation of multilayer film stacks (Fig. 2c) and the transfer of larger-scale thin films (Fig. 2d, e). Despite cracks, wrinkles and folds observed at film edges, the transferred material remains flat and continuous. Notably, free-standing membranes form readily from the solution phase after simple drop-casting across empty 5-μm wells, exhibiting excellent formability. The scanning electron microscopy (SEM) top view and cross-sectional views after focused ion beam (FIB) cutting (Fig. 2f) show an absence of scattering defects caused by polycrystalline abrasions or imperfections, supporting our highly ordered parallel stacking model (Fig. 1b).

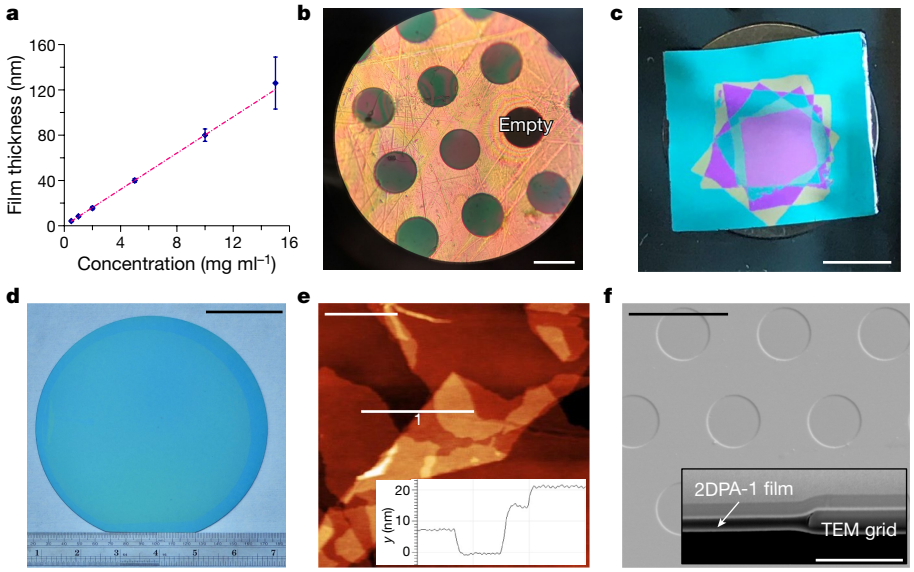

Fig. 2 | Characterization of 2DPA-1 nanofilms. a, Plot of nanofilm thickness against solution concentration of spin-coating. **b**, Transferred 2DPA-1 films across 30-μm holes. **c**, A five-layer film stack on a SiO_2/Si wafer. **d**, A 7-nm thick transferred film on a 6-inch (150 mm) wide SiO_2/Si wafer. **e**, Cracks, wrinkles and folds are observed at the film edge of **d**. The height profile of line 1 is shown in the inset. **f**, SEM images of a suspended 2DPA-1 film on an Si_3N_4 TEM grid. Inset, a cross-sectional view of a hole after focused ion beam (FIB) cutting. Scale bars are 30 μm (**b**), 5 mm (**c**), 5 cm (**d**), 1 μm (**e**) and 10 μm and 1 μm (**f** and inset, respectively).

We find that when excited at 532 nm with a polarized laser, the 2DPA-1 in powder form exhibits broad visible fluorescence at 580 nm with an apparent isotropic polarization. Meanwhile, the spin-coated nanofilm has a different fluorescent emission at 680 nm when the excitation is orthogonal to the film surface, also with isotropic polarization (Fig. 3a). However, when excitation is parallel to the film surface, the emission shifts back to 580 nm and shows a strong polarization with a clear twofold symmetry (Fig. 3b). The polarized emission maximum observed when the excitation is within the plane of the film—compared to its isotropy when perpendicular—is consistent with 2DPA-1 platelets oriented parallel to the substrate with a transition dipole along the long axis of the platelet. This molecular picture is further supported by grazing-incidence wide-angle X-ray scattering, in which a diffuse arc in the q_z axis is observed, confirming an interlayer spacing in the z direction (Fig. 3c). Its peak around 1.69 $Å^{-1}$ in the 1D profile (Fig. 3d) corresponds to a spacing of 3.72 Å, which is close to our AFM observation (Fig. 1d). These results suggest that spin-coated 2DPA-1 film consists of discotic-shaped platelets aligned parallel to the substrate surface (Fig. 1b), consistent with our AFM topology (Extended Data Fig. 2e, f).

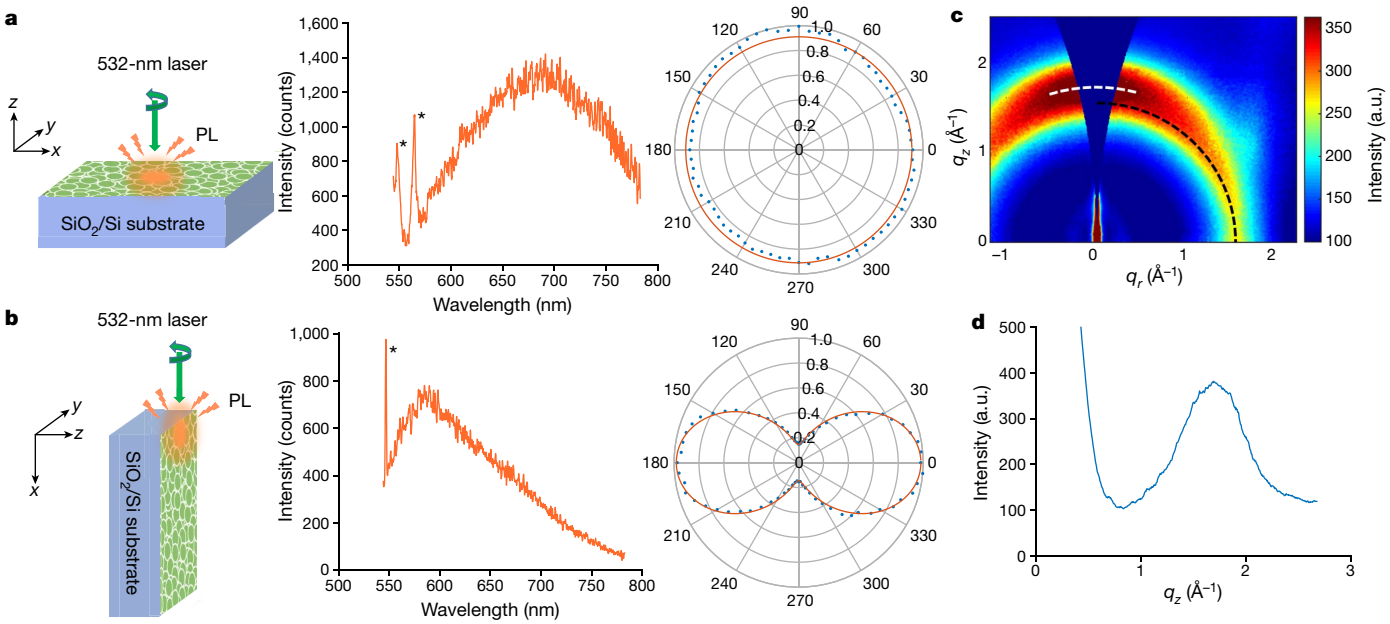

Fig. 3 | Molecular alignment in 2DPA-1 nanofilms. a, **b**, Top view (**a**) and side view (**b**) photoluminescence (PL) measurement of a 2DPA-1 nanofilm. Left, schematic illustrations; middle, photoluminescence spectra, where Si Raman peaks at 550 nm and 570 nm are labelled with '*'; right, polar plots. The red fitting curve in the polar plots gives an intensity of 0.91 (top view, **a**) and $0.1452 + 0.8365(\cos\theta)^2$ (side view, **b**). **c**, **d**, Grazing-incidence wide-angle X-ray scattering 2D image (**c**), and its 1D intensity profile near $q_r = 0$ $Å^{-1}$ (**d**) of the 2DPA-1 film. In **c**, the white dotted curve gives the diffuse arc from platelet stacking and the black dotted curve is the amorphous diffraction ring. a.u., arbitrary units.

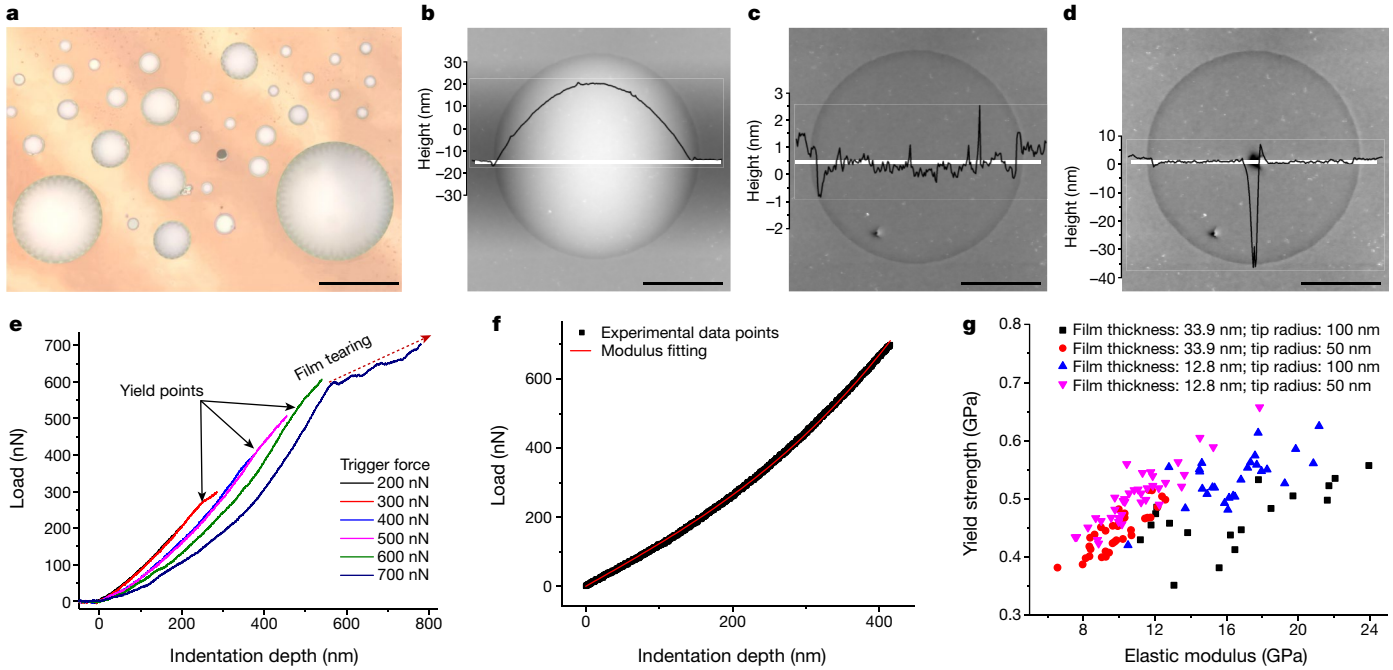

Fig. 4 | Mechanical properties of 2DPA-1 nanofilms. a, Optical micrograph of a 2DPA-1 film on a holey substrate. **b**, A 13.7-μm well is covered by a 12.8-nm thick film, forming an impermeable bubble as shown by the AFM height profile. **c**, Collapsed membrane after puncturing, showing a flat height profile. The pinhole is in the lower left. **d**, Membrane after indenting at its centre and its height profile along the white line. **e**, Indentation on a 12.8-nm thick, 13.2-μm wide free-standing membrane with different trigger forces. The tip radius is 100 nm. **f**, A representative force–displacement curve and its modulus fitting. **g**, Plot of 2D elastic modulus versus 2D yield strength of 2DPA-1 for various film thicknesses and tip radii. Scale bars are 50 μm (**a**) and 5 μm (**b**–**d**).

The interlayer hydrogen bonding for 2DPA-1 should translate into mechanical properties that approach those of oriented platelet ensembles composed of 2D van der Waals materials[25]. We measured mechanical properties of nanofilms on well defined holey substrates by AFM nanoindentation[3] (Fig. 4a). We also observe that trapped air underneath membranes from film transferring (Fig. 4b) enables measurement of 2DPA-1 permeability via the bulge test, similar to those previously reported for graphene[26,27]. Estimates from the lack of appreciable deflation place the air permeability of 2DPA-1 at least 22.8 times lower (Extended Data Fig. 4) than the most impermeable 1D barrier material[28]. This finding supports the observation of highly aligned and immobilized networks in which the molecular nanopores and intermolecular voids are not accessible to ambient gases, consistent with the low BET surface area. Puncturing the bubble with an AFM tip at the periphery releases the trapped air, yielding a flat, self-tensioned membrane (Fig. 4c). The pinholes stay localized throughout the indentation measurements (Fig. 4d), suggesting a degree of defect tolerance that is not observed in conventional 2D materials[3].

We studied 120 pierced membranes from two samples using two spherical AFM probes with different tip radii. Membranes are indented multiple times at the film centre with different trigger forces. For all membranes, we observed no ultimate failure at the force curve limit but note several inconspicuous yield points and a continuous breaking process (Fig. 4e). Small plastic deformations shift subsequent force curves toward higher strain. Therefore, the 2D Young's modulus (E^{2D}) is obtained from the elastic region corresponding to the first set of overlapping curves. The 2D yield strength (σ^{2D}) is further determined from $(FE^{2D}/4\pi R)^{1/2}$, where R is the tip radius and F is the force at the first yield point.

The average modulus of 2DPA-1 from nanoindentation is 12.7 ± 3.8 GPa, substantially higher than conventional unoriented thermoplastics (for example, polycarbonate, 2.4 GPa), crosslinked polymers (for example, toughened epoxy, 2.5 GPa), or oriented linear thermoplastics (for example, nylon, 5 GPa), approaching that of 2D crystal covalent organic framework membrane[29] (10.38 GPa). As noted, an additional advantage of 2D polymers is that they exhibit isotropic stiffness within the 2D plane, doubling the effective stiffness when compared to 1D polymer counterparts that reinforce in only a single direction[30]. 2DPA-1 also exhibits an excellent yield strength of 488 ± 57 MPa, almost twice that of structural steel (ASTM A36, 250 MPa), despite having approximately one-sixth the density (Supplementary Table 3).

We further studied the mechanical response using conventional tensile testing methods. Our previously established scroll fibre platform offers an opportunity to translate microscale mechanical properties into macro measurable quantities, and thus study material behaviour in real applications[31]. After layering a 2DPA-1 film onto a polycarbonate (PC) film and scrolling the resulting nanocomposite into an Archimedean fibre (Extended Data Fig. 5), we found that composite fibres exhibit much higher elastic moduli and tensile strength than PC controls, even at very low volume fraction (Extended Data Fig. 6). For instance, a 6.9% fraction of 2DPA-1 film enhances the fibre modulus by 72%, and the strength raises from 110 MPa to 185 MPa. Additionally, fibres do not undergo 'telescoping', an unscrolling phenomenon observed for graphene/PC scroll fibres with low initial modulus[31] (Extended Data Fig. 5c). The integrity of 2DPA-1 composites suggests a high density of interfacial polar bonds available for adhesion to the matrix, providing a considerable advance in mechanical performance compared to nanocomposites reinforced with inorganic van der Waals nanoplatelets.

In conclusion, here we report on an irreversible, solution-phase polymerization that promises new families of mechanically and chemically stable 2D polymeric materials, analogous in properties to their 1D organic counterparts. Unlike reversible synthetic routes, our approach is amenable to organic chemistry instead of a crystallization or CVD process. We find, as predicted[30] that this polyaramid system has excellent mechanical properties, almost two times stronger than structural steel, exhibiting great potential for lightweight composites. Furthermore, the ultralow gas permeability enables applications as barrier coatings and

gas selective membranes with defined structure. We envisage that this 2D polyaramid system described herein could be further structurally tuned, paving the way for a new generation of polymers for structural reinforcement, nanofiltration and gas separations.

Online content

Any methods, additional references, Nature Research reporting summaries, source data, extended data, supplementary information, acknowledgements, peer review information; details of author contributions and competing interests; and statements of data and code availability are available at https://doi.org/10.1038/s41586-021-04296-3.

1. Sakamoto, J., van Heijst, J., Lukin, O. & Schlüter, A. D. Two-dimensional polymers: just a dream of synthetic chemists? *Angew. Chem. Int. Ed.* **48**, 1030–1069 (2009).
2. Schlüter, A. D., Payamyar, P. & Öttinger, H. C. How the world changes by going from one- to two-dimensional polymers in solution. *Macromol. Rapid Commun.* **37**, 1638–1650 (2016).
3. Lee, C., Wei, X., Kysar, J. W. & Hone, J. Measurement of the elastic properties and intrinsic strength of monolayer graphene. *Science* **321**, 385–388 (2008).
4. Pop, E., Varshney, V. & Roy, A. K. Thermal properties of graphene: fundamentals and applications. *MRS Bull.* **37**, 1273–1281 (2012).
5. Stupp, S. I., Son, S., Lin, H. C. & Li, L. S. Synthesis of two-dimensional polymers. *Science* **259**, 59–63 (1993).
6. Grill, L. et al. Nano-architectures by covalent assembly of molecular building blocks. *Nat. Nanotechnol.* **2**, 687–691 (2007).
7. Kissel, P. et al. A two-dimensional polymer prepared by organic synthesis. *Nat. Chem.* **4**, 287–291 (2012).
8. Kissel, P., Murray, D. J., Wulftange, W. J., Catalano, V. J. & King, B. T. A nanoporous two-dimensional polymer by single-crystal-to-single-crystal photopolymerization. *Nat. Chem.* **6**, 774–778 (2014).
9. Kory, M. J. et al. Gram-scale synthesis of two-dimensional polymer crystals and their structure analysis by X-ray diffraction. *Nat. Chem.* **6**, 779–784 (2014).
10. Kandambeth, S., Dey, K. & Banerjee, R. Covalent organic frameworks: chemistry beyond the structure. *J. Am. Chem. Soc.* **141**, 1807–1822 (2019).
11. Diercks, C. S. & Yaghi, O. M. The atom, the molecule, and the covalent organic framework. *Science* **355**, eaal1585 (2017).
12. Baek, K. et al. Free-standing, single-monomer-thick two-dimensional polymers through covalent self-assembly in solution. *J. Am. Chem. Soc.* **135**, 6523–6528 (2013).
13. Gee, G. & Rideal, E. K. Reaction in monolayers of drying oils I—the oxidation of the maleic anhydride compound of β-elaeostearin. *Proc. R. Soc. Lond. A* **153**, 116–128 (1935).
14. Ozaki, H. et al. Formation of atomic cloth observed by Penning ionization electron spectroscopy. *J. Chem. Phys.* **103**, 1226–1228 (1995).
15. Zhong, Y. et al. Wafer-scale synthesis of monolayer two-dimensional porphyrin polymers for hybrid superlattices. *Science* **366**, 1379–1384 (2019).
16. Côté, A. P. et al. Porous, crystalline, covalent organic frameworks. *Science* **310**, 1166–1170 (2005).
17. Berlanga, I. et al. Delamination of layered covalent organic frameworks. *Small* **7**, 1207–1211 (2011).
18. Zhang, B. et al. Crystalline dioxin-linked covalent organic frameworks from irreversible reactions. *J. Am. Chem. Soc.* **140**, 12715–12719 (2018).
19. Guan, X. et al. Chemically stable polyarylether-based covalent organic frameworks. *Nat. Chem.* **11**, 587–594 (2019).
20. Cai, Z., Liu, B., Zou, X. & Cheng, H. M. Chemical vapor deposition growth and applications of two-dimensional materials and their heterostructures. *Chem. Rev.* **118**, 6091–6133 (2018).
21. Zhang, G., Zeng, Y., Gordiichuk, P. & Strano, M. S. Chemical kinetic mechanisms and scaling of two-dimensional polymers via irreversible solution-phase reactions. *J. Chem. Phys.* https://doi.org/10.1063/5.0044050 (2021).
22. Payamyar, P., King, B. T., Öttinger, H. C. & Schlüter, A. D. Two-dimensional polymers: concepts and perspectives. *Chem. Commun.* **52**, 18–34 (2016).
23. Varoon, K. et al. Dispersible exfoliated zeolite nanosheets and their application as a selective membrane. *Science* **334**, 72–75 (2011).
24. Yeh, T.-M., Wang, Z., Mahajan, D., Hsiao, B. S. & Chu, B. High flux ethanol dehydration using nanofibrous membranes containing graphene oxide barrier layers. *J. Mater. Chem. A* **1**, 12998–13003 (2013).
25. Li, P. et al. In situ nanomechanical characterization of multi-layer MoS_2 membranes: from intraplanar to interplanar fracture. *Nanoscale* **9**, 9119–9128 (2017).
26. Bunch, J. S. et al. Impermeable atomic membranes from graphene sheets. *Nano Lett.* **8**, 2458–2462 (2008).
27. Sun, P. Z. et al. Limits on gas impermeability of graphene. *Nature* **579**, 229–232 (2020).
28. Leterrier, Y. Durability of nanosized oxygen-barrier coatings on polymers. *Prog. Mater Sci.* **48**, 1–55 (2003).
29. Fang, Q. et al. Strong and flaw-insensitive two-dimensional covalent organic frameworks. *Matter* **4**, 1017–1028 (2021).
30. Sandoz-Rosado, E., Beaudet, T. D., Andzelm, J. W. & Wetzel, E. D. High strength films from oriented, hydrogen-bonded "graphamid" 2D polymer molecular ensembles. *Sci. Rep.* **8**, 3708 (2018).
31. Liu, P. et al. Layered and scrolled nanocomposites with aligned semi-infinite graphene inclusions at the platelet limit. *Science* **353**, 364–367 (2016).

Publisher's note Springer Nature remains neutral with regard to jurisdictional claims in published maps and institutional affiliations.

© The Author(s), under exclusive licence to Springer Nature Limited 2022

Methods

Synthesis of 2DPA-1

A 40-ml vial equipped with a stir bar was added with 126 mg of melamine (1 mmol, 1 equiv.), and 265 mg of trimesic acid trichloride (1 mmol, 1 equiv.), followed by 9 ml of *N*-methyl-2-pyrrolidone and 1 ml of pyridine. The mixture was stirred at room temperature (20–25 °C). After 16 h, the whole reaction mixture became a gel. This gel was cut into small pieces and then soaked in ethyl alcohol (80 ml), followed by 30-min bath sonication (if necessary). The resulting cloudy mixture was further filtrated or centrifuged, followed by deionized H_2O (80 ml) and acetone (80 ml) washing. A pale-yellow powder (228 mg, 81%) was received after house-vacuum drying at 100 °C for 16 h.

Synthesis of TMS-2DPA-1

10 mg of 2DPA-1 was added into a 4-ml glass vial, followed by 2 ml of $CHCl_3$, excess amount of trimethylsilyl trifluoromethanesulfonate (0.3 ml) and triethylamine (0.5 ml). The mixture was stirred at room temperature until a black homogenous solution was formed. Owing to the unstable nature of TMS-protected compounds, this reaction solution was diluted without any purification and directly deposited onto mica for subsequent AFM characterization.

Acyl residue fraction measurement

After synthesis, the reaction mixture was quenched with 40 ml of isopropyl alcohol. The resulting slurry was stirred for at least 3 h and then purified to give the isopropyl-terminated 2DPA-1. Dissolving the product in trifluoroacetic acid (TFA) allows ^{1}H NMR, offering the desired acyl residue-to-monomer ratio.

Preparation of 2DPA-1 nanofilms

2DPA-1 powder was dissolved in TFA, forming a homogenous solution. The 2DPA-1 solution was added to the top of a clean SiO_2-covered (300 nm) Si wafer. Then this wafer was spun at 2000 rpm for 1 min, giving a uniform nanofilm. Its thickness can be measured by AFM at scratches made by a fine needle.

Atomic force microscopy

AFM imaging was performed on Asylum Research instruments (Cypher S and MFP-3D) and a Bruker Veeco Multimode 8 instrument in a.c. mode using various probes (Arrow UHF, NPG-10, AC-160 and FASTSCAN-D-SS) for different tasks. Data were processed using the Gwyddion software package and the built-in software of the instruments.

Nanoindentation was performed on a Cypher S instrument. Si holey substrates were fabricated by photolithography and diamond-like spheric probes (NT_B50_v0010 and NT_B100_v0010, Biosphere) were purchased from Nanotool AFM Probes. Film thicknesses were obtained by taking an average at seven different positions nearby the place of interest. After manual calibration, the membrane of interest was imaged under tapping mode and punctured at its periphery under contact mode. Then the tip was moved to the film centre and nanoindentations were performed with different trigger forces. The loading force–displacement curves were extracted and analysed, giving the intrinsic 2D modulus and yield strength of 2DPA-1.

Polarized photoluminescence measurement

The entire optical set-up is shown in Extended Data Fig. 7. A continuous-wave 532-nm laser (35-072, Edmund) was used for excitation. The incident light travelled through a linear polarizer and a half-wave plate (mounted on a motorized stage) and focused onto the sample using an objective lens (Zeiss, 100×, and numerical aperture 0.75). The angle of the half-wave plate was adjusted to maximize photoluminescence intensity. Then, the stage was moved a few μm away because 2DPA-1 had already photobleached to some extent during the focusing and adjustment of the half-wave plate. The signal was collected with a spectrometer (Acton SpectraPro SP-2150, Princeton Instruments, and PyLon). The excitation power for photoluminescence measurements was 500 μW and the exposure time was 10 s. For the simple photoluminescence measurement, a spectrometer was used for data collection. However, for the polarized photoluminescence study, we used an EMCCD camera (iXon3, Andor), which is much more sensitive, to trace a longer time course despite the photobleaching of 2DPA-1. The polarity of the incident light was controlled by rotating the half-wave plate and the photoluminescence signal was collected every 5 degrees with 5 s exposure time. The excitation power was 2 μW for excitation polarization. All measurements were conducted at room temperature under air.

Scrolled fibre tensile test

The tensile test was performed on an 8848 Micro Tester (Instron). First, the scrolled fibre was glued onto a hollow cardboard using epoxy resin, with a gauge length of 16 mm. Then the whole sample was mounted onto the micro tester, and the connecting parts on the cardboard were cut, leaving a free-standing scroll fibre. The test was carried out at room temperature with a strain rate of 0.1 mm s^{-1} using a 10-N load cell. The force–displacement curve was recorded until the fibre broke off.

Data availability

The data that support the findings of this study are available from the corresponding author upon reasonable request.

Acknowledgements Membraackackackne fabrication, permeability testing and transport analysis of 2DPA-1 was supported by the Center for Enhanced Nanofluidic Transport (CENT), an Energy Frontier Research Center sponsored by the US Department of Energy (DOE), Office of Science, Basic Energy Sciences under award #DE-SC0019112. The synthetic chemistry and mechanical testing aspects of this work were funded by the Army Research Laboratory under cooperative agreement W911NF-18-2-0055. H.J.K. holds a Career Award at the Scientific Interface from the Burroughs Wellcome Fund, which supported the molecular modelling aspects of this work. We acknowledge fabrication support from the Center for Nanoscale Systems at Harvard, a member of the National Nanotechnology Coordinated Infrastructure Network (NNCI), which is supported by the National Science Foundation under NSF award no. 1541959. This research used beamline 11-BM Complex Materials Scattering (CMS) of the National Synchrotron Light Source II (NSLS-II) and the Center for Functional Nanomaterials (CFN), both of which are US DOE Office of Science User Facilities operated for the DOE Office of Science by Brookhaven National Laboratory under contract no. DE-SC0012704. We thank E. Tsai for her assistance in performing experiments at the beamline, R. Verduzco for beamline access, A. Penn and E. Brignole for MIT.Nano assistance for STEM and Cryo EM, and S. Xin Li for discussions on 2D membrane properties. We acknowledge MIT.Nano facilities and the Cypher VRS DURIP award (N000142012203) for the support on AFM characterizations. M.K. acknowledges support by the German Research Foundation (DFG) Research Fellowship KU 3952/1-1.

Author contributions Y.Z. and M.S.S. conceived and designed the reaction system, with initial laboratory synthesis and characterization of 2DPA-1 performed by Y.Z. Characterization using HR-AFM measurement and other imaging tools, and subsequent data analysis, was performed by Y.Z., P.G., X.G. and J.T. P.L., A.T.L., and J.F.Y. offered substrates for AFM characterization. Post-synthesis modification for molecular imaging and intermediate characterization was performed by Y.Z.; M.Q. and D.J.L. contributed to data analysis. Y.Z. and M.S.S. designed and developed the NMR characterization technique for defect quantification. Y.Z., M.Q. and G.Z. performed budge tests. Z. Yuan, G.Z., G.H. and M.Q. calculated permeabilities for 2DPA-1 from bulge test results. Y.Z. performed nanoindentation tests at MIT with complementary measurements from E.D.W. and E.S.-R. at ARL. Substrates for nanoindentation tests are designed and fabricated by M.K. Y.Z. designed and T.I. conducted polarized photoluminescence measurements. Y.Z. measured mechanical properties of scrolled fibres. G.Z., D.K., J. Yang, M.S.S. and H.J.K. contributed theory and material simulation. Z. Yang and H.J.K. performed molecular structure calculations for 2DPA-1. Y.Z. and M.S.S. co-wrote the manuscript with input from all other authors.

Competing interests The authors declare no competing interests.

Additional information
Supplementary information The online version contains supplementary material available at https://doi.org/10.1038/s41586-021-04296-3.
Correspondence and requests for materials should be addressed to Michael S. Strano.
Peer review information *Nature* thanks the anonymous reviewers for their contribution to the peer review of this work.
Reprints and permissions information is available at http://www.nature.com/reprints.

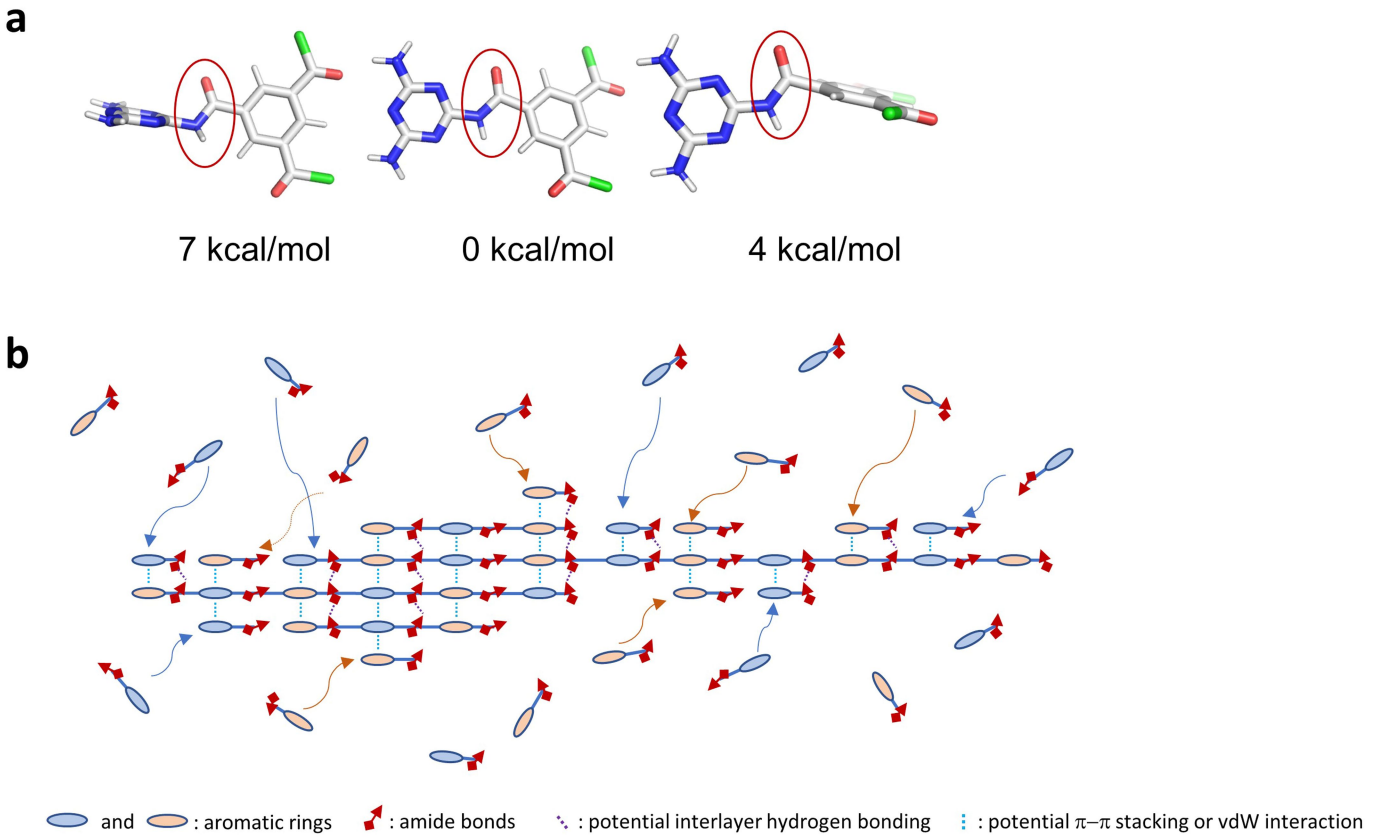

Extended Data Fig. 1 | Schematic illustration of rotation suppression and auto-catalysis. a, Linkage-core conjugations inhibit out-of-plane rotation. **b**, Auto-catalytic self-templating. Computational method: gas-phase geometry optimizations with Q-Chem v4.2 to compute 298 K conjugation enthalpies using the ωB97-XD/6-311 + $G(d,p)$ DFT functional and basis set combination.

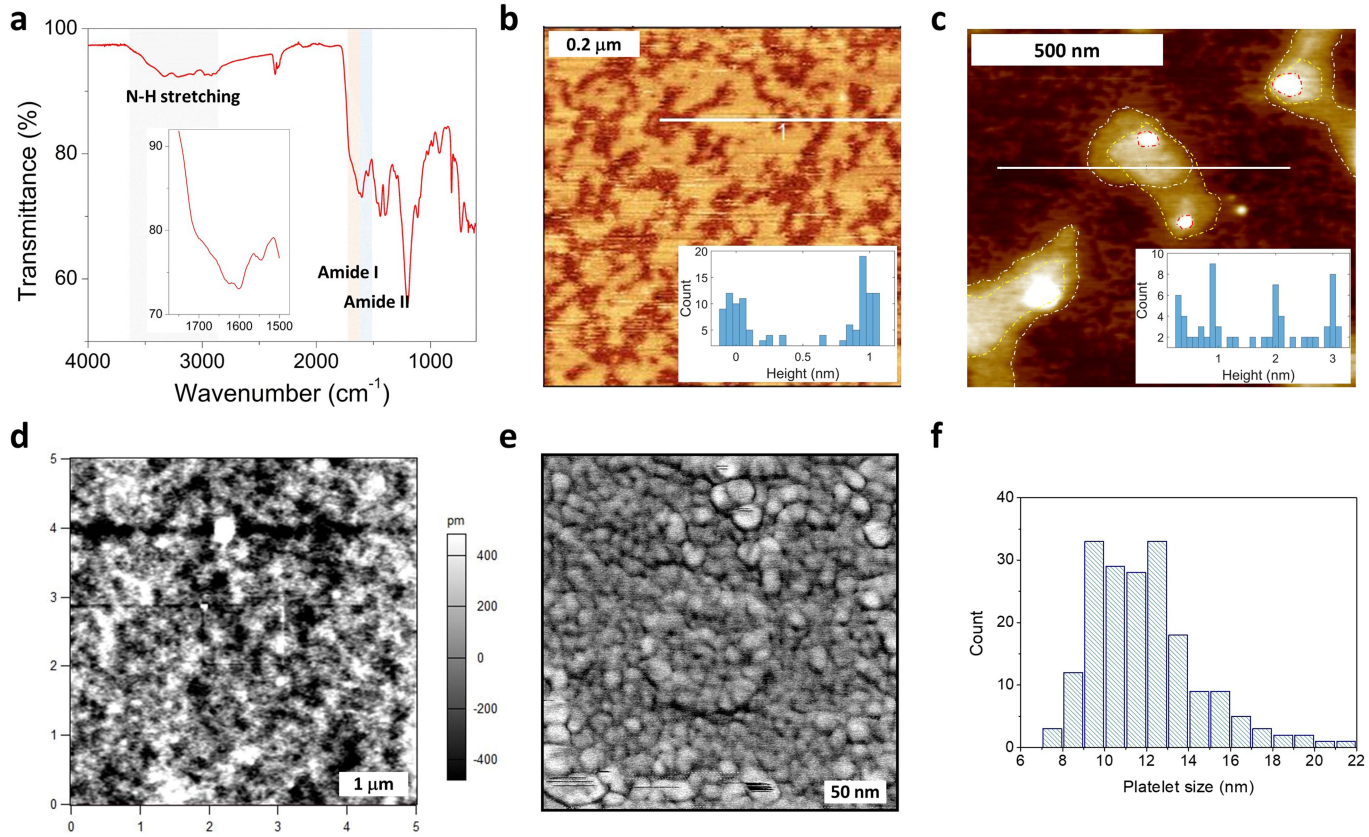

Extended Data Fig. 2 | Characterization of 2DPA-1. a, Fourier-transform infrared (FTIR) spectrum of as-synthesized 2DPA-1 powder. **b**, Atomic force microscopy (AFM) image of bilayer nanoclusters and its height histogram along the white line (inset). **c**, AFM image of stacked nanosheets; inset shows its height histogram along the white line. **d**, AFM surface topology of a spin-coated film. **e**, AFM image from amplitude channel at its second eigenmode, obtained from a film surface. **f**, The size distribution obtained from **e**.

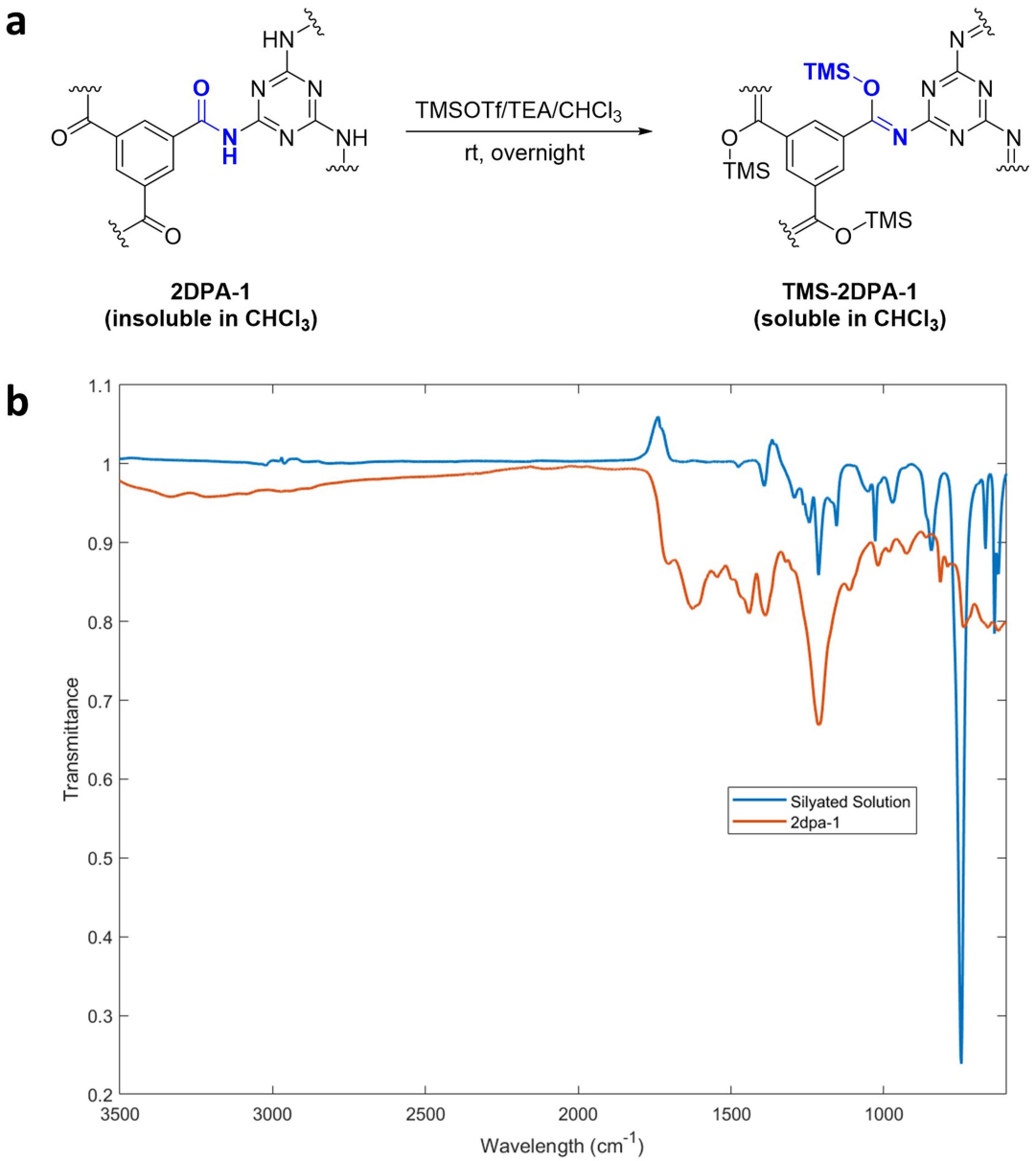

Extended Data Fig. 3 | Silylation of 2DPA-1. a, Synthetic scheme of the silylation reaction. **b**, FTIR spectra of reaction mixture and its starting material. rt, room temperature; TMSOTf, trimethylsilyl trifluoromethanesulfonate; TEA, triethylamine.

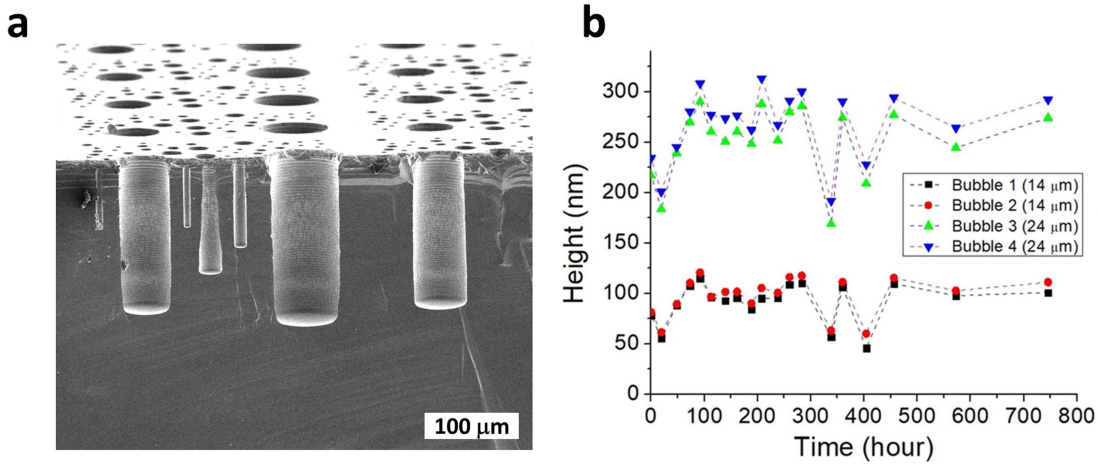

Extended Data Fig. 4 | Bulge test of 2DPA-1 films for air permeability. a, Cross-sectional view of a clean holey substrate. **b**, Bubble height versus time. Film thickness is 12.8 nm.

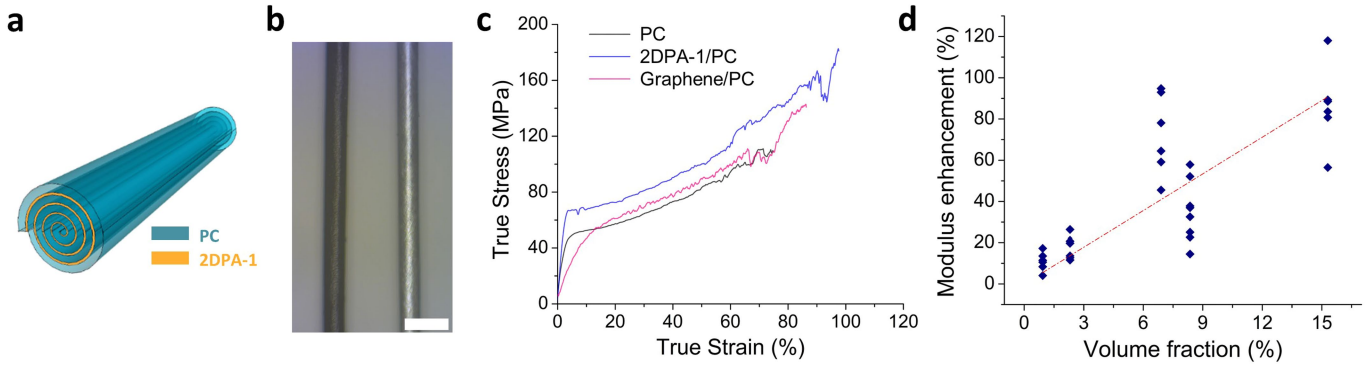

Extended Data Fig. 5 | Scrolled fibre tensile test of 2DPA-1 composites. **a**, Schematic illustration of an Archimedean scroll fibre. **b**, Optical micrograph of a hair (left) and a scrolled fibre (right). Scale bar, 100 mm. **c**, Representative true stress–strain curves from a 2D composite scrolled fibre, its polycarbonate (PC) control fibre, and a graphene/PC composite fibre (data reproduced from ref. [31]). The volume fraction for 2DPA-1/PC is 6.9% and for graphene/PC it is 0.19%. **d**, Plot of modulus enhancement ($(E - E_{PC})/E_{PC}$) versus different volume fractions of 2DPA-1.

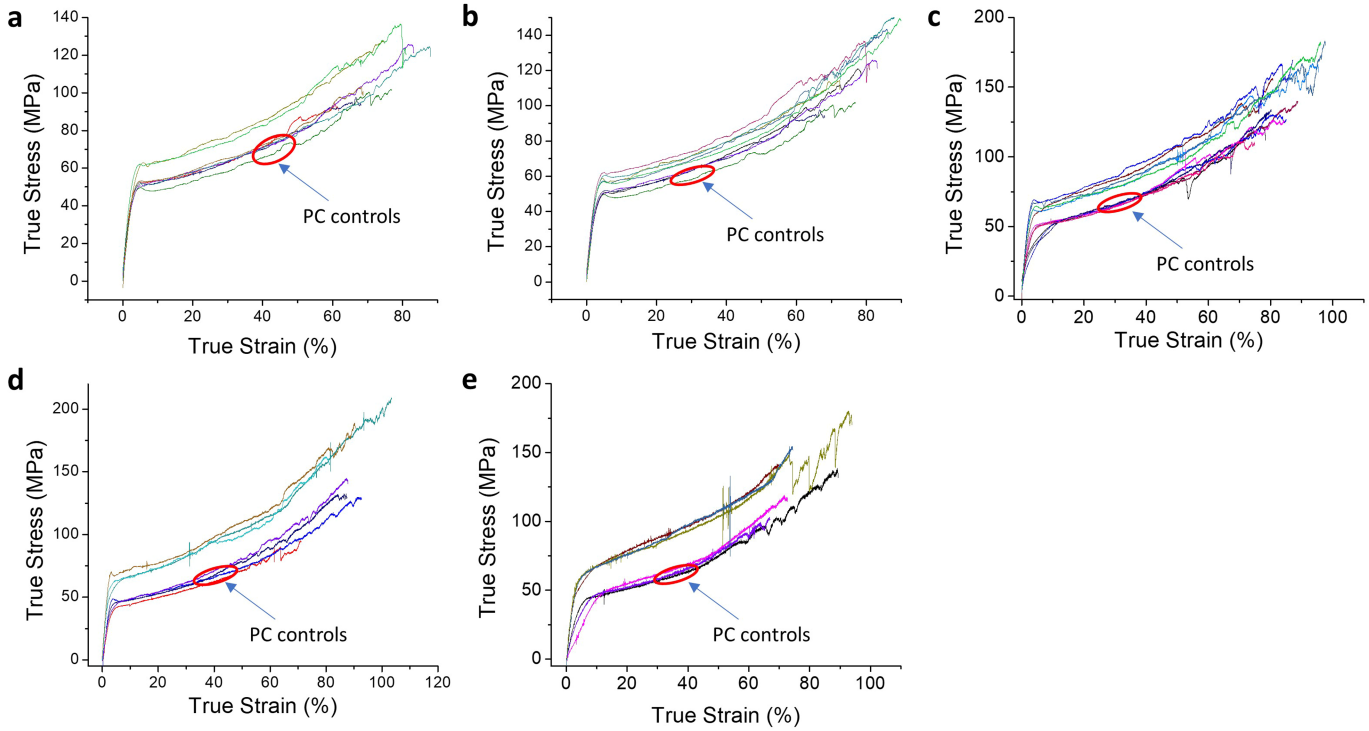

Extended Data Fig. 6 | True stress–strain plots of composite scrolled fibres and their PC controls. a, Volume fraction (V_{2DP}) = 0.9%. **b**, V_{2DP} = 2.3%. **c**, V_{2DP} = 6.9%. **d**, V_{2DP} = 7.7%. **e**, V_{2DP} = 13.3%.

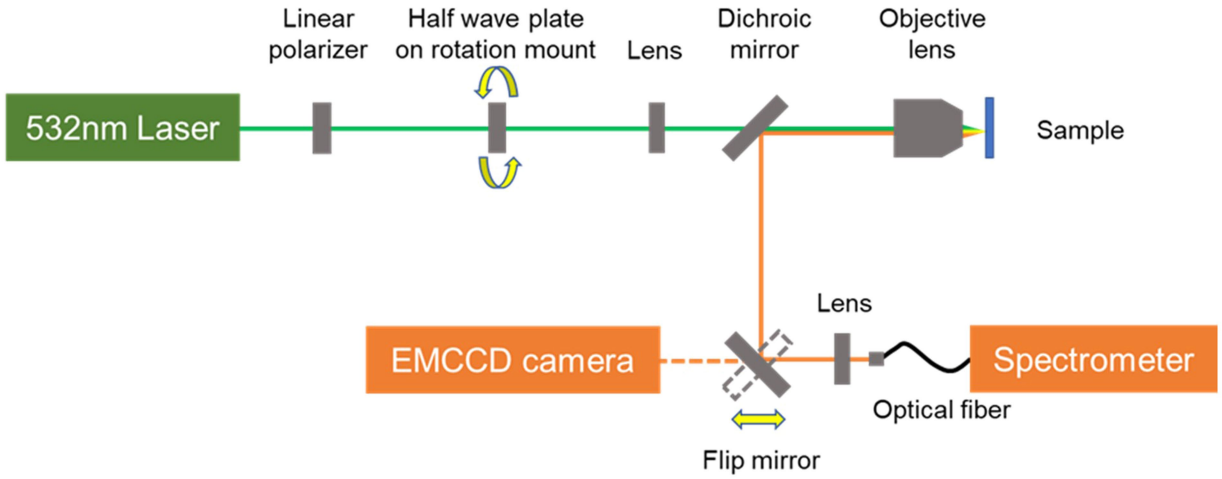

Extended Data Fig. 7 | Optical set-up for photoluminescence measurements. Excitation wavelength 532 nm, excitation power 500 μW for photoluminescence measurements, and 2 μW for excitation polarization. EMCCD, electron-multiplying charge-coupled device.